RSC Advances

PAPER

View Article Online
View Journal | View Issue

Cite this: *RSC Adv.*, 2017, **7**, 23083

Multi-wavelength excited white-emitting $K_2Gd_{(1-x)}(PO_4)(WO_4):xDy^{3+}$ phosphors with satisfactory thermal properties for UV-LEDs

Yue Guo,[a] Byung Kee Moon,[a] Byung Chun Choi,[a] Jung Hyun Jeong *[a] and Jung Hwan Kim[b]

A series of novel phosphate–tungstate phosphors, $K_2Gd_{(1-x)}(PO_4)(WO_4):xDy^{3+}$ ($0 \leq x \leq 0.07$), were synthesized successfully *via* a conventional solid-state reaction method for the first time. XRD, GSAS Rietveld refinement, FT-IR, Raman, diffuse reflectance spectra, luminescent spectra, and thermal quenching were applied to investigate the phase, structure, luminescence and thermal stability properties. The results showed that the Dy^{3+}-activated $K_2Gd(PO_4)(WO_4)$ phosphor could absorb wavelengths from the UV to the blue region, and emit blue (~480 nm), yellow (~570 nm) and red (~650 nm) light from the f–f transitions of Dy^{3+} ions. The dominant energy transfer mechanism for Dy^{3+} ions was dipole–dipole interaction. An analysis of the thermal quenching indicated that the obtained phosphors have excellent thermal stability. As the temperature increased to 423 K (150 °C), the emission intensity of the KGPW:0.05Dy^{3+} phosphor with 388 nm excitation still retained about 76.8% of its initial intensity at room temperature. In addition, the color purity of $K_2Gd_{0.995}(PO_4)(WO_4):0.005Dy^{3+}$ was calculated to be 90% with a correlated color temperature of 5569 K. Therefore, these results suggest that multi-wavelength excited $K_2Gd_{(1-x)}(PO_4)(WO_4):xDy^{3+}$ phosphors may have potential to be candidates for white LEDs for lighting and optical display applications.

Received 23rd February 2017
Accepted 13th April 2017

DOI: 10.1039/c7ra02242e

rsc.li/rsc-advances

1. Introduction

During the past few decades, solid state white light-emitting diodes (w-LEDs) have been drawing worldwide attention as next generation lighting devices due to their extraordinary advantages, such as high electro-optical conversion efficiency, high brightness, low power consumption and environmental benefits.[1–5] Up until now, the most common strategy of w-LEDs is the combination of a blue InGaN chip (450–470 nm) and yellow emitting $Y_3Al_5O_{12}:Ce^{3+}$ (YAG:Ce^{3+}) phosphor.[6] However, this strategy couldn't meet the general illumination requirements long-term due to the low color rendering index (CRI) and the high correlated color temperature (CCT), which restrict its further application.[4] This problem may be solved by the combination of a near-UV LED chip with tri-color (red, green and blue) phosphors.[7,8] Nevertheless, in this tri-color phosphor system, the luminescence efficiency is relatively low since the blue emission is strongly reabsorbed by the green and red phosphors.[9] Besides, the device of multiple emitting components in this system is very complicated and expensive, and it is also difficult to control the color balance. Compared with these methods, doping a single rare earth ion into an appropriate host is still the simplest and most straightforward method to obtain white light.

As we know, among rare earth ions, trivalent dysprosium (Dy^{3+}) ion, which has a $4f^9$ electron configuration, can achieve most easily white light emission since the emission properties usually consist of three characteristic emission bands: one in the blue region (~480 nm), one in the yellow region (~580 nm), and last one in the red region (~650 nm), originating from $^4F_{9/2} \rightarrow {}^6H_{15/2}$, $^4F_{9/2} \rightarrow {}^6H_{13/2}$, and $^4F_{9/2} \rightarrow {}^6H_{11/2}$ transitions, respectively. Therefore, by suitably tuning the yellow-to-blue (Y/B) intensity ratio, Dy^{3+} ions have significant potentialities to obtain white light emission. Owing to the prominence of white light emittance from Dy^{3+} ions, many researchers have spent a large amount of manpower and materials to explore the luminescence properties of Dy^{3+} ions in various hosts. Recently, we have manufactured some novel and promising Dy^{3+}-activated single phase white-emitting phosphors matched with near-UV chips possessing potential application prospects in display and lighting.[10–12]

To date, a novel phosphate–tungstate family compound, $M_2Ln(PO_4)(WO_4)$ (M = Na, K; Ln = Y, Gd, Lu), has been used as host materials due to its easy synthesis, low sintering temperature, good thermal stability and high quenching concentration.[1,13] In $K_2Ln(PO_4)(WO_4)$ crystal structure, the $[Ln^{3+}–O^{2-}–Ln^{3+}]$ unit is isolated by the surrounding $[PO_4]^{3-}$ and $[WO_4]^{2-}$ units in the three-dimensional network. This special lattice

[a]*Department of Physics, Pukyong National University, Busan 608-737, South Korea. E-mail: jhjeong@pknu.ac.kr; Fax: +82 51 629 5549; Tel: +82 51 629 7388*
[b]*Department of Physics, Dongeui University, Busan 614-714, South Korea*

arrangement reveals that the interaction between the Ln^{3+}–Ln^{3+} layers might be blocked, which cause the high quenching concentration phenomenon. For $K_2Ln(PO_4)(WO_4)$:Tb^{3+},Eu^{3+} (Ln = Y, Gd and Lu), the critical concentration of Tb^{3+} or Eu^{3+} is as high as 40–50% in the singly doped phosphor.[1] However, in $K_2Y(WO_4)(PO_4)$:Tm^{3+},Dy^{3+}, the critical concentration of Tm^{3+} or Dy^{3+} is 1% and 5%, respectively.[14] Such a large quenching difference in the same type of structure is not only the problem of the host but also the rare earth ions. Additionally, there are one independent K^+ site, one independent P^{5+} site, one independent W^{6+} site and one independent Ln^{3+} site in $K_2Ln(PO_4)(WO_4)$ unit cell. Considering the valence states and ionic radius of Ln^{3+} and Dy^{3+} ions, it is deduced that the Dy^{3+} ions easy to occupy Ln^{3+} sites.[14]

To the best of our knowledge, the studies on the luminescent properties of Dy^{3+}-activated $K_2Gd(PO_4)(WO_4)$ phosphor are sparse.[1,14] In this work, the structural, detailed luminescent properties, and thermal stabilities were applied to characterize the obtained phosphors. The emission color were located in the warm white-emitting region under near-UV excitation. In addition, compared with some other inorganic materials, the obtained phosphors exhibit a more excellent thermal stability. It is noteworthy that co-doped phosphor system severely affected by part of the energy loss due to the role of energy transfer, which is common in co-doped system. However, single-doped phosphor system can suppress the above situation, meanwhile it may have potential use in w-LEDs or some other areas.

2. Experimental

2.1 Materials and synthesis

The powder samples of the phosphate-tungstate $K_2Gd_{(1-x)}(PO_4)(WO_4)$:$xDy^{3+}$ (x = 0, 0.005, 0.01, 0.02, 0.03, 0.05 and 0.07) compound were prepared by solid state synthesis as follows. In the synthesis, all raw materials K_2CO_3 (99.90%), Gd_2O_3 (99.99%), $(NH_4)_2HPO_4$ (99.90%), WO_3 (99.99%) and Dy_2O_3 (99.99%) were used as received and weighed following the stoichiometric ratio. Firstly, the mixture were ground together about 30 min in an agate mortar. Secondly, the mixture based precursors were slowly pre-sintered at 500 °C (in air) and kept this temperature for 3 h to remove the chemically combined water and ammonium gas, as well as decompose the carbonate. After that, the samples were re-sintered at 950 °C (in air) for 3 h. At last, the obtained samples were ground well into powder for further characterization. The Dy^{3+}-activated $K_2Gd(PO_4)(WO_4)$ phosphor was supplied by the display and Lighting Phosphor Bank at Pukyong National University.

2.2 Material characterization

The phase purity was carefully verified by using powder X-ray diffraction (XRD) measurement collected on a D8 Advanced diffractometer operated at 40 kV, 30 mA with Ni-filtered Cu-Kα irradiation (λ = 1.5406 Å). The powder diffraction patterns of $K_2Gd_{0.995}(PO_4)(WO_4)$:$0.005Dy^{3+}$ for Rietveld analysis was collected with a PANalytical X'Pert³ Powder instrument, the step size of 2θ was 0.013° over the angular range $10° \leq 2\theta \leq 80°$. Crystal structure refinement employed the Rietveld method as implemented in the General Structure Analysis System (GSAS) software suite.[15] Transmission electron microscopy observations (TEM) were performed on JEM-2010 electron microscope with an accelerating voltage of 200 kV. The diffuse reflectance spectra (DRS) were recorded on a V-670 UV-vis spectrophotometer (JASCO Corp., Japan) ranging from 200 to 700 nm. The Fourier transform infrared spectroscopy (FT-IR) spectra were collected on a FT-IR spectrophotometer (FT/IR-4000, JASCO, Japan) over a frequency range 650–4000 cm^{-1}. The Raman spectrometry measurements were carried out with a 532 nm laser JASCO NRS-5100 instrument. The photoluminescence excitation (PLE) and emission (PL) spectra were measured by using a Photon Technology International (PTI, USA) fluorimeter equipped with a 60 W xenon lamp excitation source. The fluorescence lifetime curves were measured with a phosphorimeter attached to the fluorescence spectrophotometer with a 25 W xenon flash lamp. The PL quantum efficiency (QE) was measured by using a spectrofluorometer (JASCO, FP-8500, Japan) equipped with an integrating sphere attachment (ISF-834). The color coordinates in Commission Internationale de l'Eclairage (CIE) 1931 chromaticity diagram were calculated from emission spectra by the color calculator software. The temperature-dependent luminescence properties were measured on a fluorescence spectrophotometer (SCINCO FS-2) with a heating apparatus (NOVA ST540).

3. Results and discussion

3.1 Phase formation and structural characteristics of $K_2Gd(PO_4)(WO_4)$

The XRD patterns of $K_2Gd_{(1-x)}(PO_4)(WO_4)$:$xDy^{3+}$ (abbreviated as KGPW:xDy^{3+}) phosphors, which the standard PDF file is not available, with different contents of Dy^{3+} ions are displayed in Fig. 1(a). By comparing all the diffraction peaks, no more impurities or raw materials were detected, indicating that those solid solutions are of phase purity and the single-doped Dy^{3+} ions do not cause any detectable change in KGPW host structure. Fig. 1(b) shows the observed and calculated XRD patterns of the GSAS Rietveld refinement for KGPW:$0.005Dy^{3+}$ sample. The initial structural model for the refinement was established by the standard crystallographic data of $K_2Ho(PO_4)(WO_4)$ (ICSD#206654) compound which has an orthorhombic structure with space group *Iabc*.[16] All the atom positions, fraction factors, thermal vibrational parameters, and background were converged and refined. The crystallographic data is presented in Table 1 and the refined atomic coordinate parameters are presented in Table 2. It can be observed that the final refined R factors converged to R_{wp} = 9.38%, R_P = 6.35%, indicating that the solid solution KGPW:$0.005Dy^{3+}$ shares the same structure with $K_2Ho(PO_4)(WO_4)$. In addition, the lattice parameters converged to a = 6.8794(2) Å, b = 12.1534(9) Å, c = 19.6921(4) Å, and V = 1646.442 Å^3. Fig. 2 shows the elemental mapping of KGPW:$0.03Dy^{3+}$ phosphor, revealing that the elements of K, Gd, P, W, O and Dy are uniformly distributed over the whole particle.

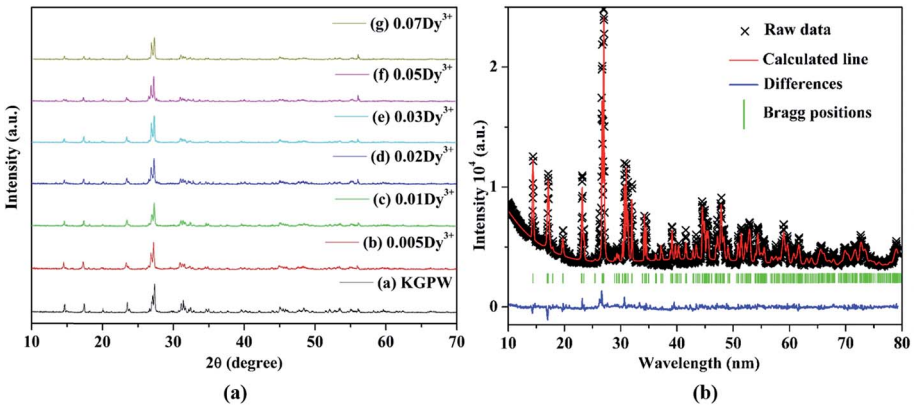

Fig. 1 (a) XRD patterns of KGPW phosphors with different contents of Dy^{3+} ions. (b) Observed (crosses) and calculated (solid lines) XRD patterns of the Rietveld refinement for KGPW:0.005Dy^{3+} sample.

Table 1 The crystallographic data and selected bond lengths of KGPW:0.005Dy^{3+} sample

Crystallographic data of KGPW:0.005Dy^{3+}		Selected bond length (Å)			
X-ray source	CuKα	Ln–O(1, 1′)	2.3819(25)	K–O(2)	2.9844(6)
T/K	295	Ln–O(3, 3′)	2.3850(8)	K–O(2′)	3.1908(6)
Symmetry	Orthorhombic	Ln–O(4, 4′)	2.3123(11)	K–O(2″)	2.7177(6)
Space group	*Ibca*	Ln–O(4″, 4‴)	2.5290(8)	K–O(3)	2.7225(4)
a/Å	6.8794(2)	P–O(3, 3′)	1.54447(28)	K–O(3′)	2.7887(4)
b/Å	12.1534(9)	P–O(4″, 4‴)	1.58154(27)	K–O(4″)	3.0945(7)
c/Å^3	19.6921(4)	W–O(1, 1′)	1.8400(4)	Ln–Ln	4.0330(6)
Volume/Å^3	1646.442	W–O(2, 2′)	1.7540(4)		
R_p	6.35%	Ln–P_1	3.2160(9)		
R_{wp}	9.38%	Ln–P_2	2.9710(9)		
χ^2	4.24%	Ln–K	3.8427(28)		

Fig. 3 shows the crystal structure of KGPW:0.005Dy^{3+} obtained from GSAS refinement file. In KGPW:0.005Dy^{3+}, two successive $[WO_4]^{2-}$ layers form a tungstate zigzag viewed from the *a*-axis, Ln^{3+} layer and $[PO_4]^{3-}$ layer are ordered alternately along the *b*-axis as shown in Fig. 3(a and b). Therefore, the Ln^{3+} layer is isolated by two successive $[WO_4]^{2-}$ layers on the *a*-axis and $[PO_4]^{3-}$ layer on the *b*-axis in this three-dimensional network. This special lattice arrangement reveals that the interaction between the Ln^{3+}–Ln^{3+} layers might be blocked. However, Fig. 3(b and c) show the Ln^{3+}–Ln^{3+}(Dy^{3+}–Dy^{3+}) unit sharing two oxygen atoms (O_4′ and O_4′), which is close to each other. This will causes the interaction among Ln^{3+}–Ln^{3+} units greatly enhanced as the doping concentration increasing. For KGPW:0.005Dy^{3+} sample, the selected bond lengths from the GSAS refinement are listed in Table 1. The Ln cation located at 8d position, which contains a mixture of 99.5% Gd and 0.5% Dy, is coordinated by eight oxygen atoms with two WO_4 units and four PO_4 units as shown in Fig. 3(d). The Ln–O bond lengths range from 2.3 to 2.5 Å, resulting in an irregular polyhedron.

Table 2 Refined atomic coordinate parameters for KGPW:0.005Dy^{3+} sample as determined by Rietveld refinement of the powder XRD data at room temperature

Atom	Wyck	*x*/*a*	*y*/*b*	*z*/*c*
W_1	8e	0.5000(0)	0.2500(0)	0.3325(4)
Ln_1	8d	0.7500(0)	0.3303(7)	0.5000(0)
K_1	16f	0.9687(2)	0.0799(2)	0.3438(9)
P_1	8d	0.7500(0)	0.0704(2)	0.5000(0)
O_1	16f	0.7088(0)	0.2796(0)	0.3853(6)
O_2	16f	0.4420(0)	0.3643(0)	0.2845(0)
O_3	16f	0.7308(0)	−0.0047(0)	0.4383(4)
O_4	16f	0.9229(0)	0.1514(0)	0.4921(5)

3.2 Photoluminescence characteristics

In order to characterize the existence of $[PO_4]^{3-}$ and $[WO_4]^{2-}$ units in our obtained samples, the FT-IR spectrum of the pure KGPW is measured and showed in Fig. 4(a). One can see that there are four strong infrared absorption peaks located at 786, 843, 962 and 1081 cm^{-1}. In general, the IR absorption bands of $[PO_4]^{3-}$ are located at 650–540 cm^{-1} and 1120–940 cm^{-1}, originating from the symmetric stretching mode of the $[PO_4]^{3-}$ units.[17] Thus, two infrared absorption peaks at 962 and 1081 cm^{-1} are coming from $[PO_4]^{3-}$ units. Besides, the other peaks at 786 and 843 cm^{-1} are assigned to the stretching modes of $[WO_4]^{2-}$ units.[18] These results indicate that $[PO_4]^{3-}$ and $[WO_4]^{2-}$ units exist in our obtained sample, which can be deduced in all samples.

Fig. 4(b) shows the Raman spectrum of the pure KGPW sample in the region of 200–1200 cm^{-1}. In free space, $[WO_4]$

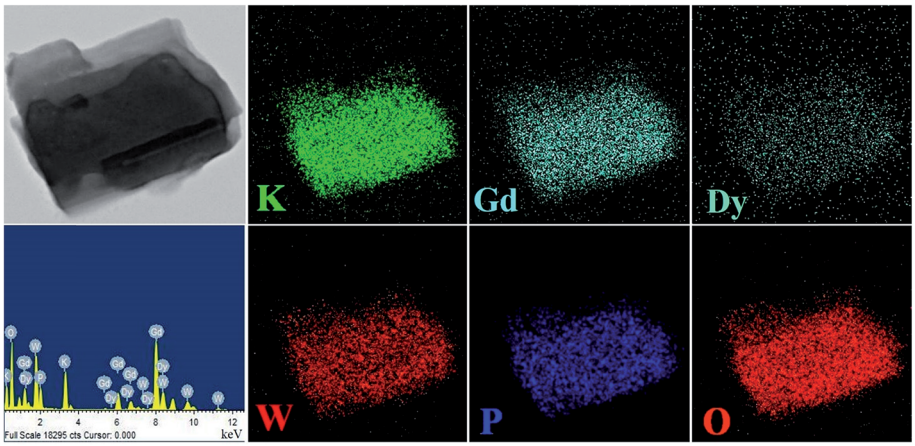

Fig. 2 Elemental mapping of the KGPW:0.03Dy^{3+} phosphor.

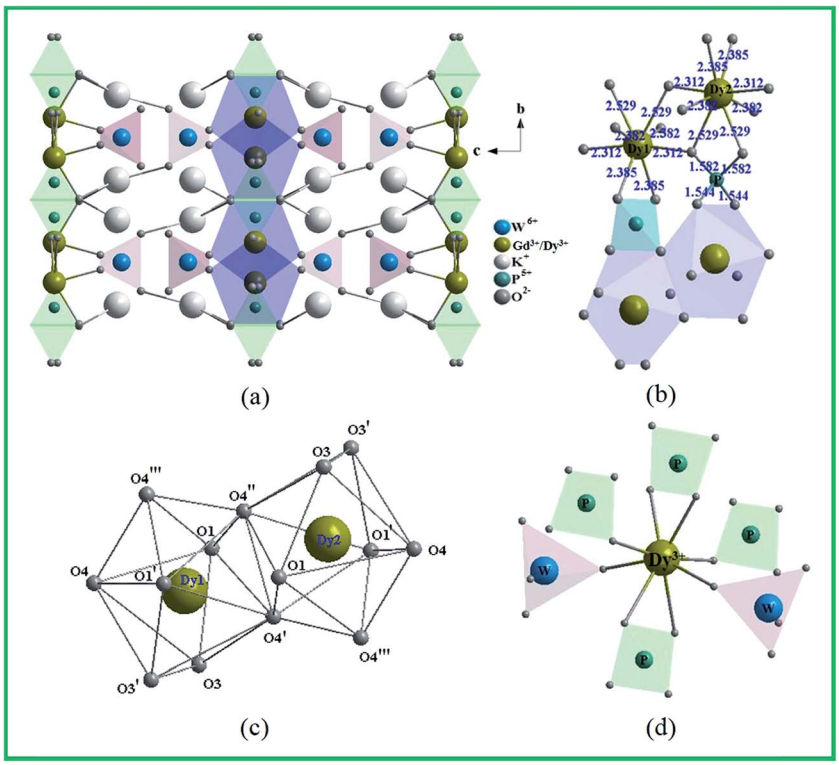

Fig. 3 Crystal structure of KGPW:0.005Dy^{3+}. (a) Viewed from the *a*-axis, (b) the polyhedral links between DyO_8 and PO_4 units, (c) two DyO_8 units with eight-oxygen coordination atoms, (d) the coordination environment of Dy^{3+} site.

tetrahedron has T_d symmetry.[19,20] The basic vibration modes from $[WO_4]^{2-}$ units have four internal modes: υ_1 (A1), υ_2 (E), υ_3 (F2) and υ_4 (F2). As shown in Fig. 4(b), the strong Raman vibration peak located at 936 cm^{-1} is assigned to the W–O symmetric stretching vibration υ_1 (A1). The Raman peak at 327 cm^{-1} is attached to O–W–O symmetric bending vibration υ_2 (E) while these peaks at 729, 821 and 856 cm^{-1} are designated as W–O anti-symmetric stretching vibration υ_3 (F2), and peaks at 354 and 380 cm^{-1} should be assigned as O–W–O anti-symmetric bending vibration υ_4 (F2). Additionally, $[PO_4]^{3-}$ tetrahedron with T_d symmetry possesses the same four internal vibration modes. The Raman peak at 978 cm^{-1} corresponds to the symmetric stretching vibration of P–O, and two weak Raman peaks located at 1048 and 1082 cm^{-1} are specified as anti-symmetric stretching vibration of P–O. Since $[PO_4]^{3-}$ unit is trapped between two DyO_8 layers, the symmetric and anti-symmetric bonding vibrations almost limited. As shown in the enlarged image on Fig. 4(b), the weak Raman peak at 551 cm^{-1} is assigned as O–P–O symmetric bending vibration, and the other two peaks at 594 and 633 cm^{-1} are classified as W–O anti-symmetric stretching vibration.

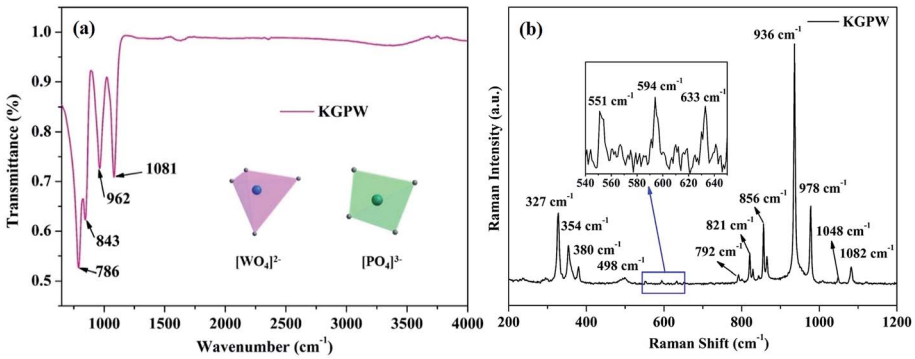

Fig. 4 FT-IR spectrum (a) and Raman spectrum (b) of the pure KGPW sample.

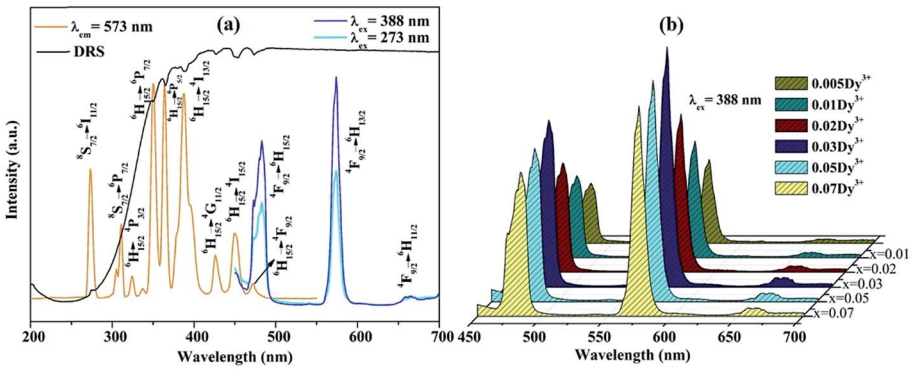

Fig. 5 (a) The PLE and PL spectra, as well as UV-vis DRS of KGPW:0.005Dy^{3+}, (b) the PL spectra of KGPW:xDy^{3+} ($x = 0.005$, 0.01, 0.02, 0.03, 0.05 and 0.07).

The PLE spectrum (monitored at 573 nm) and the PL spectra (excited at 273 and 388 nm) of KGPW:0.005Dy^{3+} sample, as well as UV-vis DRS are shown in Fig. 5(a). The UV-vis DRS shows a broad absorption band at 200–330 nm and several small absorption bands ranging from 350 to 480 nm. The broad absorption band is attributed to the charge transfer from the oxygen ligands to the central tungsten atom inside the $[WO_4]^{2-}$ unit. Besides, several small absorption bands are from f–f transitions of Dy^{3+} ions, which share the same positions with the results from PLE spectrum as shown in Fig. 5(a). In the PLE spectrum, two sharp bands at 273 and 313 nm are from $^8S_{7/2} \rightarrow {}^6I_{11/2}$ and $^8S_{7/2} \rightarrow {}^6P_{7/2}$ transitions of Gd^{3+} ions, respectively. Other bands at 324, 350, 364, 388, 426, 450 and 472 nm are originating from $^6H_{15/2} \rightarrow {}^4P_{3/2}$, $^6H_{15/2} \rightarrow {}^6P_{7/2}$, $^6H_{15/2} \rightarrow {}^6P_{5/2}$, $^6H_{15/2} \rightarrow {}^4I_{13/2}$, $^6H_{15/2} \rightarrow {}^4G_{11/2}$, $^6H_{15/2} \rightarrow {}^4I_{15/2}$, and $^6H_{15/2} \rightarrow {}^4F_{9/2}$ f–f transitions of Dy^{3+} ions.[21] The energy levels of Dy^{3+}-activated KGPW sample is presented in Fig. 6(a). All observed peaks of the sample could be found. It is noteworthy that those

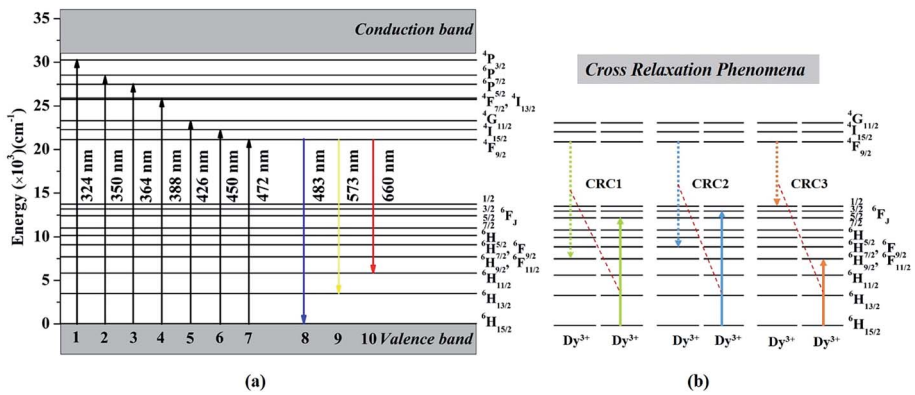

Fig. 6 (a) Energy levels of Dy^{3+} ions, (b) three possible cross-relaxation processes among Dy^{3+} ions.

solid solutions match well with the commercial near-UV chips, suggesting its promising application in phosphor-converted white LEDs. Under 388 nm excitation, the PL spectrum shows three emission bands at 483, 573, and 660 nm originating from $^4F_{9/2} \rightarrow {}^6H_{15/2}$, $^4F_{9/2} \rightarrow {}^6H_{13/2}$, and $^4F_{9/2} \rightarrow {}^6H_{11/2}$ transitions of Dy^{3+} ions, respectively. It is well-known that the $^4F_{9/2} \rightarrow {}^6H_{15/2}$ transition following the selection rules which is insensitive to the crystal field strength around the Dy^{3+} ions. While the $^4F_{9/2} \rightarrow {}^6H_{13/2}$ transition is attributed to forced electric dipole transition which is strongly influenced by the surrounding environment.[22,23] The $^4F_{9/2} \rightarrow {}^6H_{13/2}$ transition is only allowed at low symmetry with no inversion center. Therefore, when Dy^{3+} ions occupy low symmetry local site, the yellow prevails. In contrast, the blue emission is dominant. From the PL spectra (see Fig. 5(b)), it is clear that yellow emission intensity is much stronger than that of the blue emission, indicating that Dy^{3+} ions reside in a low symmetry site. In addition, under 273 nm excitation the PL spectrum shows the duplicate three emission bands, demonstrating the energy transfer from Gd^{3+} to Dy^{3+} ions could be occurred.

In order to further explore the effect of different Dy^{3+} doping concentrations, a series of KGPW:xDy^{3+} (x = 0.005, 0.01, 0.02, 0.03, 0.05 and 0.07) phosphors were synthesized and measured as shown in Fig. 5(b). We can see that the emission intensity of Dy^{3+} rises first as gradual increase Dy^{3+} doping concentration until the maximum value x at 0.03 and then drops with the similar profile. Fig. 7 shows the optimum concentration for Dy^{3+}-activated KGPW samples is 0.03 mol. This low concentration quenching phenomenon is not consistent with the previously reported by Wen *et al.*[1] As far as we know, the possible reason for the low concentration quenching phenomenon in the obtained phosphors is the cross-relaxation mechanism between neighboring Dy^{3+} ions. As shown in Fig. 3(b) and Table 1, the Ln–Ln distance along the b-axis is close enough to 4.033 Å. Considering the energy match rule, Fig. 6(b) presents the following three possible cross-relaxation channels (CRC) among Dy^{3+}, denoted as CRC1, CRC2 and CRC3, which are responsible for population decrease of $^4F_{9/2}$ level:

$$^4F_{9/2} + {}^6H_{15/2} \rightarrow {}^6H_{9/2}/{}^6F_{11/2} + {}^6F_{5/2}$$

$$^4F_{9/2} + {}^6H_{15/2} \rightarrow {}^6H_{7/2}/{}^6F_{9/2} + {}^6F_{3/2}$$

$$^4F_{9/2} + {}^6H_{15/2} \rightarrow {}^6F_{1/2} + {}^6H_{9/2}/{}^6F_{11/2}$$

After the above three cross-relaxation processes, the Dy^{3+} ions at $^4F_{9/2}$ levels are de-excited to ($^6H_{9/2}/{}^6F_{11/2}$), $^6H_{7/2}/{}^6F_{9/2}$) or $^6F_{1/2}$ levels, and concomitantly the ground states of neighboring Dy^{3+} ions will accept the energy and be excited to $^6F_{5/2}$, $^6F_{3/2}$ or $^6H_{9/2}/{}^6F_{11/2}$ levels. Finally, all the Dy^{3+} ions involved in these three cross-relaxation processes reach their ground states, resulting in the luminescence of the $^4F_{9/2}$ level quenched.

The concentration quenching start an effective role when exceed this optimum concentration causing decreased luminous intensity. In general, the non-radiative energy transfer among Dy^{3+} ions causing the concentration quenching is dominant, following three types of mechanisms: radiation reabsorption, exchange interaction, or a multipolar–multipole interaction.[24] In order to identify the mechanism of energy transfer, the critical distance (R_C) between the activated ions for energy transfer can be evaluated according to the equation given by Blasse:[25]

$$R_{Dy} = 2\left(\frac{3V}{4\pi x_i N}\right)^{1/3} \quad (1)$$

where N is the number of available sites of Dy^{3+} occupying per unit cell, x_i is the critical concentration of Dy^{3+}, and V is the volume per unit cell. For KGPW phosphor, $N = 8$, $V = 1646.442$ Å^3, $x = 0.03$, then the R_{Dy} is calculated to be 23.57 Å. Clearly stated, the value of R_C is significantly larger than 5 Å, indicating that multipolar–multipolar interaction type is dominated for the non-radiative energy transfer among Dy^{3+} ions.

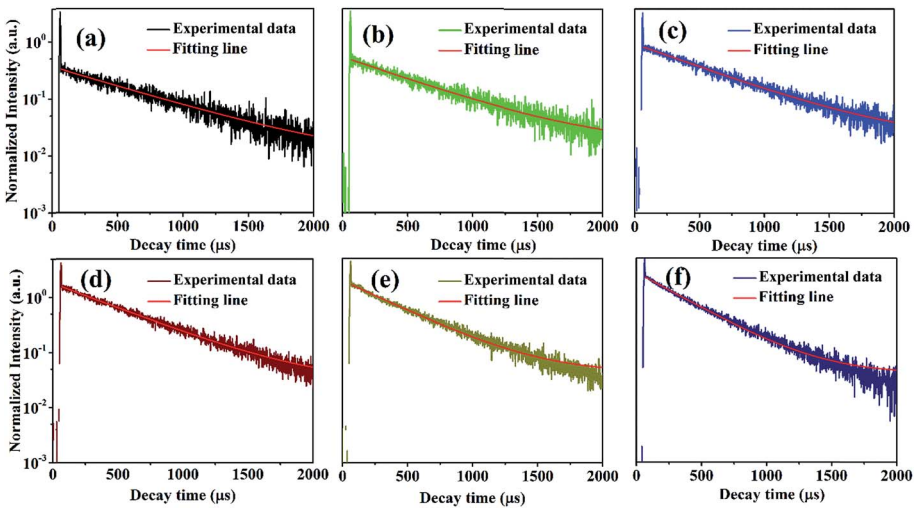

Fig. 7 Decay curves of KGPW:xDy^{3+} (x = 0.005, 0.01, 0.02, 0.03, 0.05 and 0.07) samples with 388 nm excitation by monitoring at 573 nm.

The representative PL decay curves of the Dy^{3+} ions were measured with 388 nm excitation by monitoring the emission at 573 nm as shown in Fig. 7. There is a fast decay signal at the initial time in all samples. This signal may be coming from the instrumental response. By fitting the above decay curves, the decay curves in low Dy^{3+} concentration (0.005 to 0.01, 0.02 mol) are fitted successfully on the single-exponential equation:

$$I_t = I_0 \exp(-t/\tau) \quad (2)$$

where I_t and I_0 are the PL intensities at time t and 0, τ is the decay time. However, the decay curves are non-exponential in KGPW:xDy^{3+} ($x = 0.05$ and 0.07) samples. Moreover, their non-exponential increase as the Dy^{3+} concentration increases. The nonexponentiality of the decay curves indicates that the probability of energy transfer among Dy^{3+} ions increases with increasing Dy^{3+} concentration.[26] In order to investigate the mechanisms of Dy–Dy interaction, the evolution of the concentration of the emission decays was analyzed. Assuming that the interaction scheme is a multipolar type, Inokuti–Hirayama's formula is given by:[27]

$$\frac{I(t)}{I_0} = \exp\left[-\left(\frac{t}{\tau}\right) - \left(\frac{C}{C_0}\right)\Gamma\left(1-\frac{3}{S}\right)\left(\frac{t}{\tau}\right)^{3/S}\right] \quad (3)$$

where τ is the intrinsic lifetime of a single ion, $\Gamma(1 - 3/S)$ is the gamma function, C is the number of acceptors (quenching sites) per unit volume, $C_0 = 3/(4\pi R_c^3)$; where R_c is the critical interaction distance between Dy^{3+} and Dy^{3+} ions, S is the electric multipolar series, and the value of $S = 6$, 8, and 10 for dipole–dipole (d–d), dipole–quadrupole (d–q), quadrupole–quadrupole (q–q) interactions, respectively. To obtain the value of S, the above-mentioned eqn (3) can be rearranged as the following equation:

$$\ln\left[-\ln\left(\frac{I(t)}{I_0}\right) - \left(\frac{t}{\tau}\right)\right] \quad vs. \quad \ln\left[\frac{t}{\tau}\right]^3 \quad (4)$$

On the basis of the above eqn (4), plots of $\ln[-\ln(I(t)/I_0) - (t/\tau)]$ *vs.* $\ln[t/\tau]^3$ with the fitting line is given in Fig. 8. The slope of the fitting line is equal to $1/S$. The fitting results of KGPW:xDy^{3+}((a) $x = 0.05$ and (b) $x = 0.07$) samples are shown in Fig. 8. As can be seen from this figure, the values of S for KGPW:xDy^{3+}($x = 0.05$ and 0.07) samples were calculated to be 5.3 and 4.7, both approximated to 6. Therefore, the dominant energy transfer mechanism for Dy^{3+} ions in KGPW host is d–d interaction.

Fig. 9 presents the Commission Internationale de l'Eclairage (CIE) chromaticity diagram of KGPW:xDy^{3+} samples under 388 nm excitation. It is found that the CIE chromaticity coordinates for the Dy^{3+}-activated KGPW samples had warm white emission. The phosphor KGPW:0.005Dy^{3+} with CIE at ($x = 0.33$, $y = 0.36$) is extremely close to the National Television Standards Committee (NTSC) white point ($x = 0.33$, $y = 0.33$). The calculated T_{cct} (T_{cct}: the temperature at which a radiating black body produces the same color) values located at 5367–5574 K, which are close to that of sunlight at noon. According to the NTSC and European Broadcasting Union (EBU) standards, the color purity of phosphor is an essential technological factor for LEDs display application since it has a major impact on the color rendering

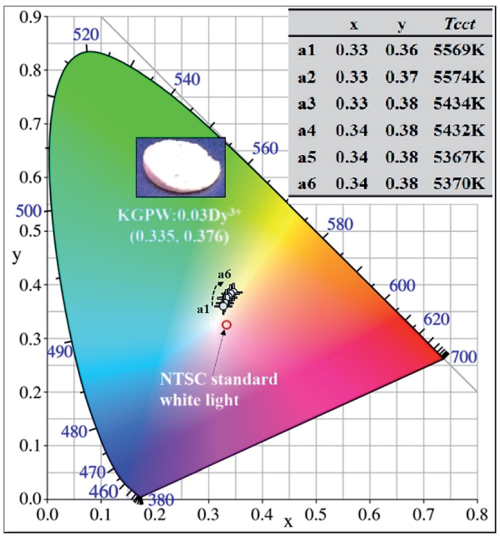

Fig. 9 The CIE chromaticity coordinates of KGPW:xDy^{3+} samples under 388 nm excitation. Inset shows the calculated CIE chromaticity coordinates and the correlated color temperatures (T_{cct}).

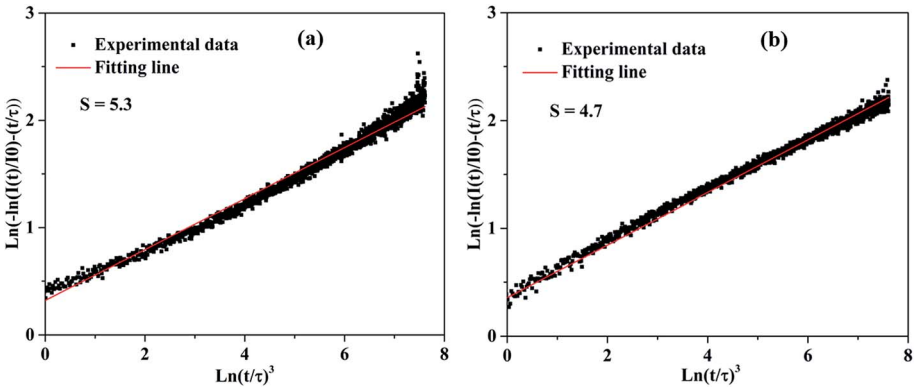

Fig. 8 The plots of $\ln[-\ln(I(t)/I_0) - (t/\tau)]$ *vs.* $\ln[t/\tau]^3$ with the fitting lines of KGPW:xDy^{3+} samples ((a) $x = 0.05$, (b) $x = 0.07$).

index and the light output. The color purity can be estimated by the following expression:[28]

$$\text{Color purity} = \frac{\sqrt{(x-x_i)^2+(y-y_i)^2}}{\sqrt{(x_d-x_i)^2+(y_d-y_i)^2}} \times 100\% \quad (5)$$

where (x, y) is the color coordinate of the sample ($x = 0.331, y = 0.364$), (x_i, y_i) is the CIE color coordinate of white illumination ($x_i = 0.333, y_i = 0.333$), and (x_d, y_d) is the CIE color coordinate of the dominant wavelength ($x_d = 0.305, y_d = 0.350$). By using the coordinates of (x, y), (x_i, y_i), (x_d, y_d), the color purity is determined to be approximately 90%, suggesting that the Dy^{3+}-activated KGPW phosphors with high purity and warm white emissions may have promising applications in w-LEDs. The QE of KGPW:0.03Dy^{3+} phosphor with the highest PL intensity is measured as 18.98%. The result is compared with the reported phosphors in Table 3.

Table 3 The internal quantum efficiency (QE) of KGPW:0.05Dy^{3+} phosphor compared with the selected results from reported references

Sample	Excitation wavelength (nm)	QE (%)	Note
KGPW:0.05Dy^{3+}	364	18.98	This work
$Ca_{2.95}Si_2O_7$:0.05Dy^{3+}	365	15.16	33
$Ca_{0.98}MoO_4$:0.02Dy^{3+},0.02K^+	351	8	34
$La_{1.95}W_2O_9$:0.05Dy^{3+}	398	21.3	35
$MgY_{3.99}Si_3O_{13}$:0.01Dy^{3+}	347	21.6	36

3.3 Thermal properties analysis

In general, phosphors suffer a decrease of emission intensity in the process of phosphors' application with temperature increasing. Therefore, the thermal stability of photoluminescence is of great significance for phosphor as it greatly affects not only the color rendering index but also the light output of w-LEDs. The temperature-dependent luminescence properties of KGPW:0.05Dy^{3+} phosphor excited at 273 and 388 nm were tracked with temperature increasing from 303 to 463 K as shown in Fig. 10(a and b). One can see that the emission intensities of KGPW:0.05Dy^{3+} sample decrease progressively with temperature increasing. Moreover, as the temperature increases to 423 K (150 °C), the emission intensities of KGPW:0.05Dy^{3+} phosphor under 273 nm and 388 nm excitation are 25.3% and 76.8% of their initial intensities at room temperature, respectively, as shown in the inset of Fig. 10(a and b). It is notable that the obtained phosphors have excellent thermal stability with 388 nm excitation, which is an essential condition for practical application.

To further understand the temperature-dependent photoluminescence properties, the activation energy of thermal quenching can be calculated from the Arrhenius equation:[29–31]

$$I = \frac{I_0}{1 + Ae^{-E_a/kT}} \quad (6)$$

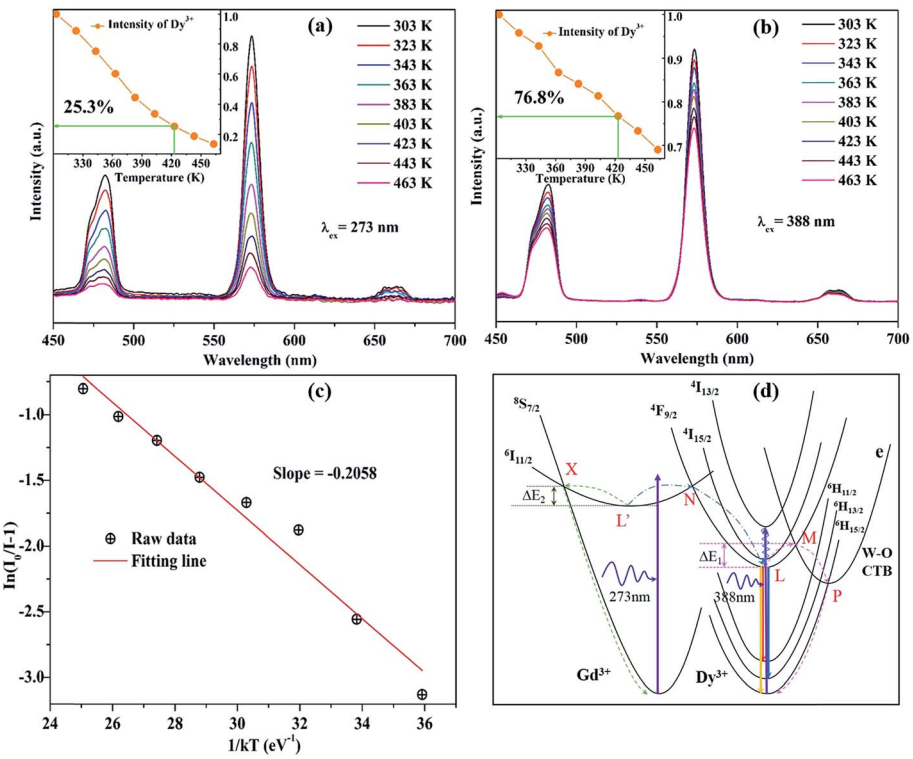

Fig. 10 The temperature-dependent luminescence properties of KGPW:0.05Dy^{3+} phosphor were tracked with temperature from 303 K to 463 K under 273 nm (a) and 388 nm (b) excitation. (c) Plots of $\ln[I_0/I - 1]$ against $1/kT$ of KGPW:0.05Dy^{3+} phosphor under 388 nm excitation. (d) The configurational coordinate diagram of the ground and excited states of Gd^{3+} and Dy^{3+}, as well as the CTB of WO_4.

in which I_0 is the initial emission intensity at room temperature and I is the emission intensity at testing temperature T (K), E_a is the activation energy for the thermal quenching, k is the Boltzmann constant (8.62×10^{-5} eV K^{-1}) and A is a constant for a certain host. The eqn (6) can be rearranged as follows:

$$\ln\left\{\frac{I_0}{I} - 1\right\} = \ln A - \frac{E_a}{kT} \quad (7)$$

Fig. 10(c) depicts plots of $\ln[I_0/I - 1]$ against $1/kT$ of KGPW:0.05Dy^{3+} phosphor under 388 nm excitation. Through a best-fit using eqn (7), the activation energy E_a for thermal quenching were deduced to be 0.2058 eV for 388 nm excitation.

The configurational coordinate diagram of the ground and excited states of Gd^{3+} and Dy^{3+}, as well as the charge transfer band (CTB) of WO_4 are displayed in Fig. 10(d). The curves of $^8S_{7/2}$ and $^6I_{11/2}$ represent the ground and excited states of Gd^{3+}, respectively. The curves of $^6H_{15/2}$–$^6H_{13/2}$–$^6H_{11/2}$ and $^4F_{9/2}$–$^4I_{15/2}$–$^4I_{13/2}$ represent the ground and excited states of Dy^{3+}, respectively. The curves e represents the excited state of CTB of WO_4 units. Points L and L′ are the lowest states positions of $^4F_{9/2}$ and $^6I_{11/2}$, respectively. X and N are the crossing points of $^6I_{11/2}$ to $^8S_{7/2}$ and to $^4F_{9/2}$ states, M and P are the crossing points of $^4F_{9/2}$ to e and e to $^6H_{15/2}$, respectively. Under the excitation of 388 nm, the electrons in $^6H_{15/2}$ ground state absorb the energy and transfer it to $^4I_{13/2}$ excited state at room temperature. Then, the electrons of Dy^{3+} at $^4I_{13/2}$ state undergo a non-radiative process relaxing to the $^4F_{9/2}$, from where the electrons return to the ground state $^6H_{15/2}$–$^6H_{13/2}$–$^6H_{11/2}$ by radiative transition. With the increase of temperature, the phonon vibration is strengthened and the electrons at the lowest excited state ($^4F_{9/2}$) L position can absorb the phonon energy ΔE_1. Simultaneously, the electrons excited from point L to M, then drops to P, from where the electrons undergo a non-radiative process relaxing to $^6H_{15/2}$, leading to the rapid decrease of electron number. Besides, under the excitation of 273 nm, the electrons in $^8S_{7/2}$ ground state of Gd^{3+} absorb the energy and be excited to $^6I_{11/2}$ state at room temperature. Then, the electrons cross point N showing energy transfer from Gd^{3+} to Dy^{3+} ions. As the temperature increases, the phonon vibration is strengthened and the electrons at the lowest excited state ($^6I_{11/2}$) L′ position will be likely to overcome the phonon energy ΔE_2 relaxed to the ground state ($^8S_{7/2}$). This process greatly reduced the energy transfer from Gd^{3+} to Dy^{3+} causing the rapid luminescence quenching of Dy^{3+}, which indicates that energy transfer efficiency is significantly influenced by temperature. The energy transfer efficiency (η_T) from the Gd^{3+} to Dy^{3+} ions can be approximated calculated by the following equation:[32]

$$\eta_T = \frac{I_t}{I_0} \quad (8)$$

where I_t and I_0 are the luminescence intensity of the Dy^{3+} ion at different temperature and at room temperature, respectively. By calculation, the η_T from the Gd^{3+} to Dy^{3+}were decreased from 86.7%, 73.1%, 59.7%, 43.5%, 32.6%, 25.3%, 18.7%, to 13.5% as the temperature increases from 323 K, 343 K, 363 K, 383 K, 403 K, 423 K, 443 K, to 463 K, respectively.

In the above discussion, we have elaborated that there are significant differences in temperature-dependent photoluminescence between 273 and 388 nm excitations. Obviously, the emission intensity at 388 nm excitation is more stable than that at 273 nm excitation. When excited at 273 nm, the direct reason for the rapid luminescence quenching of Dy^{3+} is that the energy migrated from Gd^{3+} to Dy^{3+} ions greatly reduced as the temperature increases. Specifically, in the energy distribution, the level of electrons overcoming ΔE_2 increases with the temperature increasing, resulting that the number of electrons from Gd^{3+} to Dy^{3+} rapid decreases in KGPW host.

4. Conclusion

In conclusion, multi-wavelength excited white-light emitting Dy^{3+}-activated KGPW phosphors were synthesized successfully by using the solid state method. Photoluminescence properties were systematically investigated, the PLE spectrum is consisted of a series of sharp peaks ranging from 270 nm to 500 nm, which match well with the commercial near-UV chips suggesting its promising application in phosphor-converted white LEDs. Under the excitation of 388 nm, the PL spectrum shows three emission bands from $^4F_{9/2} \rightarrow {}^6H_{15/2}$ (483 nm), $^4F_{9/2} \rightarrow {}^6H_{13/2}$ (573 nm) and $^4F_{9/2} \rightarrow {}^6H_{15/2}$ (660 nm) transitions of Dy^{3+} ions. In addition, the PL spectrum shows the duplicate three emission bands upon 273 nm excitation, demonstrating the energy transfer from Gd^{3+} to Dy^{3+} ions could be occurred. The quenching concentration was found to be 0.03 mol. It is notable that, as the temperature increases to 423 K (150 °C) the emission intensities of KGPW:0.05Dy^{3+} phosphor under 273 nm and 388 nm excitation are 25.3% and 76.8% of their initial intensities at room temperature, respectively, which show the obtained phosphors have excellent thermal stability with 388 nm excitation. In addition, the Dy^{3+}-activated KGPW phosphors show high purity (90%) warm white emission. All the results indicate that the multi-wavelength excited white-emitting Dy^{3+}-activated KGPW phosphors have a potential application for white light LEDs.

Acknowledgements

This research was supported by the Basic Science Research Program through the National Research Foundation of Korea (NRF) funded by the Ministry of Science, ICT and Future Planning (No. 2015060315). The phosphate–tungstate $K_2Gd_{(1-x)}(PO_4)(WO_4):xDy^{3+}$ phosphor was supplied by the Display and Lighting Phosphor Bank at Pukyong National University.

References

1 D. Wen, J. Feng, J. Li, J. Shi, M. Wu and Q. Su, *J. Mater. Chem. C*, 2015, **3**, 2107–2114.
2 Y. Guo, B. K. Moon, B. C. Choi, J. H. Jeong and J. H. Kim, *J. Lumin.*, 2017, **181**, 96–102.
3 C. Li, J. Dai, J. Huang, D. Deng, H. Yu, L. Wang, Y. Ma, Y. Hua and S. Xu, *Ceram. Int.*, 2016, **42**, 6891–6898.
4 X. Fu, W. Lü, M. Jiao and H. You, *Inorg. Chem.*, 2016, **55**, 6107–6113.

5 T. Selvalakshmi, S. Sellaiyan, A. Uedono and A. C. Bose, *RSC Adv.*, 2014, **4**, 34257–34266.
6 H. Chen, H. Lin, J. Xu, B. Wang, Z. Lin, J. Zhou and Y. Wang, *J. Mater. Chem. C*, 2015, **3**, 8080–8089.
7 P.-P. Dai, C. Li, X.-T. Zhang, J. Xu, X. Chen, X.-L. Wang, Y. Jia, X. Wang and Y.-C. Liu, *Light: Sci. Appl.*, 2016, **5**, e16024.
8 J. Zhao, C. Guo, X. Su, H. M. Noh and J. H. Jeong, *J. Am. Ceram. Soc.*, 2014, **97**, 1878–1882.
9 M. Shang, C. Li and J. Lin, *Chem. Soc. Rev.*, 2014, **43**, 1372–1386.
10 Q. Liu, Y. Liu, Y. Ding, Z. Peng, X. Tian, Q. Yu and G. Dong, *Ceram. Int.*, 2014, **40**, 10125–10129.
11 Z. Ci, Q. Sun, S. Qin, M. Sun, X. Jiang, X. Zhang and Y. Wang, *Phys. Chem. Chem. Phys.*, 2014, **16**, 11597–11602.
12 G. Zhu, Y. Wang, Q. Wang, X. Ding, W. Geng and Y. Shi, *J. Lumin.*, 2014, **154**, 246–250.
13 M. Daub, A. J. Lehner and H. A. Höppe, *Dalton Trans.*, 2012, **41**, 12121–12128.
14 L. Han, X. Xie, J. Lian, Y. Wang and C. Wang, *J. Lumin.*, 2016, **176**, 71–76.
15 B. H. Toby, *J. Appl. Crystallogr.*, 2001, **34**, 210–213.
16 K. V. Terebilenko, I. V. Zatovsky, V. N. Baumer, N. S. Slobodyanik and O. V. Shishkin, *Acta Crystallogr., Sect. E: Struct. Rep. Online*, 2008, **64**, i75.
17 K. Li, Y. Zhang, X. Li, M. Shang, H. Lian and J. Lin, *Dalton Trans.*, 2015, **44**, 4683–4692.
18 K. K. Rasu, D. Balaji and S. M. Babu, *J. Lumin.*, 2016, **170**, 547–555.
19 S. Nishigaki, S. Yano, H. Kato, T. Hirai and T. Nonomura, *J. Am. Ceram. Soc.*, 1988, **71**, C11–C17.
20 P. Pereira, A. De Moura, I. Nogueira, M. Lima, E. Longo, P. de Sousa Filho, O. Serra, E. Nassar and I. Rosa, *J. Alloys Compd.*, 2012, **526**, 11–21.
21 D. Wang, J. Fan, M. Shang, K. Li, Y. Zhang, H. Lian and J. Lin, *Opt. Mater.*, 2016, **51**, 162–170.
22 G. B. Nair and S. Dhoble, *RSC Adv.*, 2015, **5**, 49235–49247.
23 P. S. Babu, P. P. Rao, S. Mahesh, T. L. Francis and T. Sreena, *Mater. Lett.*, 2016, **170**, 196–198.
24 Y. Guo, B. K. Moon, B. C. Choi, J. H. Jeong, J. H. Kim and H. Choi, *Ceram. Int.*, 2016, **42**, 18324–18332.
25 G. Blasse, *Phys. Lett. A*, 1968, **28**, 444–445.
26 S.-D. Jee, J. K. Park and S.-H. Lee, *J. Mater. Sci.*, 2006, **41**, 3139–3141.
27 M. Inokuti and F. Hirayama, *J. Chem. Phys.*, 1965, **43**, 1978–1989.
28 W. Xiao, X. Zhang, Z. Hao, G.-H. Pan, Y. Luo, L. Zhang and J. Zhang, *Inorg. Chem.*, 2015, **54**, 3189–3195.
29 Y. Chen, F. Pan, M. Wang, X. Zhang, J. Wang, M. Wu and C. Wang, *J. Mater. Chem. C*, 2016, **4**, 2367–2373.
30 L. Tian, J. Shen, T. Xu, L. Wang, L. Zhang, J. Zhang and Q. Zhang, *RSC Adv.*, 2016, **6**, 32381–32388.
31 Z.-C. Wu, H.-H. Fu, J. Liu, S.-P. Kuang, M.-M. Wu, J.-G. Xu and X.-J. Kuang, *RSC Adv.*, 2015, **5**, 42714–42720.
32 F. Du, W. Zhuang, R. Liu, Y. Liu, J. Zhong, P. Gao, X. Zhang, W. Gao and L. Shao, *RSC Adv.*, 2017, **7**, 1075–1081.
33 X. Zhang, Z. Lu, F. Meng, L. Hu, X. Xu, J. Lin and C. Tang, *Mater. Lett.*, 2012, **79**, 292–295.
34 S. Dutta, S. Som and S. Sharma, *RSC Adv.*, 2015, **5**, 7380–7387.
35 T. Nakajima, H. Hanawa and T. Tsuchiya, *J. Ceram. Process. Res.*, 2016, **17**, 485–488.
36 Z. Ci, R. Guan, L. Jin, L. Han, J. Zhang, J. Ma and Y. Wang, *CrystEngComm*, 2015, **17**, 4982–4986.